

Exploring the Role of Sub-micron Sized Dust Grains in the Atmospheres of Red L0 – L6 Dwarfs

^{1,2,3}Kay Hiranaka

khiranak@hunter.cuny.edu

^{1,2,3,4}Kelle L. Cruz

^{3,5}Stephanie T. Douglas

⁶Mark S. Marley

and

^{1,3,7}Vivienne F. Baldassare

ABSTRACT

We examine the hypothesis that the red near-infrared colors of some L dwarfs could be explained by a “dust haze” of small particles in their upper atmospheres. This dust haze would exist in conjunction with the clouds found in dwarfs with more typical colors. We developed a model which uses Mie theory and the Hansen particle size distributions to reproduce the extinction due to the proposed dust haze. We apply our method to 23 young L dwarfs and 23 red field L dwarfs. We

¹Hunter College, Department of Physics and Astronomy, City University of New York, 695 Park Ave, New York, NY 10065, U.S.A.

²CUNY Graduate Center, City University of New York, 365 Fifth Avenue, New York, NY 10016, U.S.A.

³American Museum of Natural History, Department of Astrophysics, Central Park West at 79th Street, New York, NY, 10024, U.S.A.

⁴Visiting Astronomer at the Infrared Telescope Facility, which is operated by the University of Hawaii under Cooperative Agreement no. NNX-08AE38A with the National Aeronautics and Space Administration, Science Mission Directorate, Planetary Astronomy Program.

⁵Columbia University, Department of Astronomy, 550 West 120th Street, Mail Code 5246, New York, NY, 10027, U.S.A.

⁶NASA Ames Research Center, MS-245-3, Moffett Field, CA 94035, U.S.A.

⁷University of Michigan, Department of Astronomy, 1085 S. University, Ann Arbor, MI, 48109, U.S.A.

constrain the properties of the dust haze including particle size distribution and column density using Markov-Chain Monte Carlo methods. We find that sub-micron range silicate grains reproduce the observed reddening. Current brown dwarf atmosphere models include large grain (1–100 μm) dust clouds but not submicron dust grains. Our results provide a strong proof of concept and motivate a combination of large and small dust grains in brown dwarf atmosphere models.

Subject headings: stars: low-mass, brown dwarfs — dust, extinction

1. Introduction and Problem

Brown dwarfs are substellar objects with intermediate masses bridging the stellar and planetary regimes. Brown dwarfs do not have high enough mass to sustain hydrogen fusion in their cores, so they keep cooling with time. As brown dwarfs age, they also contract and their surface gravities increase. The cool temperatures of brown dwarfs allow condensates to form in their atmospheres, which shape their emergent spectra (Burrows et al. 2001).

There is a wide spread in $J - K_s$ colors of L dwarfs of a given spectral type. So-called ‘red’ L dwarfs have redder-than-average near-infrared (NIR) colors, and have notably redder spectral slopes through the NIR than typical L dwarfs (Faherty et al. 2013). Low-gravity objects tend to be systematically redder but some field-aged L dwarfs also have redder colors. Red, low-gravity L dwarfs can be considered ‘exoplanet analogs’ and are of particular interest (Kirkpatrick et al. 2008; Cruz et al. 2009; Faherty et al. 2009, 2013).

While the range of NIR colors of L dwarfs has not been fully explained, it is commonly attributed to variation in metallicity, gravity, and/or cloud properties (Saumon and Marley 2008; Marley et al. 2012). Brown dwarfs are thought to have refractory particles typically ranging 1–100 μm in size in their atmospheres and these particles shape their emergent spectra (Ackerman & Marley 2001; Cushing et al. 2008). Current brown dwarf atmosphere models either use these large dust grains that are organized into discrete cloud layers, or small submicron grains that are mixed throughout the atmosphere (Allard et al. 2001). These atmosphere models reproduce the general trend of L dwarf spectra but fail to give a reasonable explanation for the observed reddening in the NIR. Model spectral energy distribution (SED) fitting sometimes gives unrealistically low gravities and small f_{sed} (cloud sedimentation efficiency parameter) values (Ackerman & Marley 2001; Cushing et al. 2008) and radii too small compared to evolutionary models (Liu et al. 2013) for red L dwarfs. A better dust treatment is needed that can account for the observed reddening in L dwarf

spectra.

In efforts to understand the red objects empirically, it has been found that dust described by the interstellar reddening law can de-redden red L dwarf spectra to look like standard objects (Looper et al. 2010; Marocco et al. 2014). Interstellar reddening is the extinction of starlight caused by the interstellar dust. The interstellar grains, which have radii less than $1\ \mu\text{m}$, suppress blue light more effectively than red light. As a result, distant stars look redder than they actually are. The interstellar reddening law (extinction law) is an empirical relationship between the extinction at any wavelength $A(\lambda)$ and the visual extinction $A(V)$ (Cardelli, Clayton, and Mathis 1989). We do not expect significant interstellar reddening in brown dwarfs since they are so close to the Sun on a galactic scale, so the use of the interstellar reddening law to de-redden brown dwarf spectra is not physically motivated. However, ISM-like grains ($< 1\ \mu\text{m}$) in the atmospheres of red L dwarfs might produce results similar to the interstellar reddening law and explain the observed reddening.

Looper et al. (2010) de-redden the optical spectra of TWA 30 (young M5 star) using the interstellar reddening law described by Cardelli, Clayton, and Mathis (1989). Although the reddening seen towards TWA 30 may be due to dust in the disk within the line of sight, Looper et al. (2010) demonstrated that the interstellar reddening law can be successfully used in this case and it can be useful for dealing with reddening due to small grains other than the interstellar medium (ISM). Marocco et al. (2014) de-redden the spectra of several L dwarfs including ULAS J222711–004547 (L7pec) using two interstellar extinction curves (Cardelli, Clayton, and Mathis 1989; Fitzpatrick 1999) and found that sub-micron size dust grains can explain the reddening effect. Furthermore, Cushing et al. (2006) ascribe a flattening in the spectra of mid-type L dwarfs seen at $9\text{--}11\ \mu\text{m}$ to a population of small silicate grains above the main cloud deck.

These three results imply that brown dwarfs with red spectral energy distributions may have small grains like the ISM which are smaller than $1\ \mu\text{m}$ in addition to larger grains ranging from $1\text{--}100\ \mu\text{m}$ currently included in the models in their atmospheres that scatter and absorb the emergent light.

In this work, we develop a prescription for a dust haze in L dwarf atmospheres and test whether it can account for the characteristics of red L dwarf spectra. By constraining the nature of this dust haze we aim to better understand the physical cause of the reddening in brown dwarfs. Independently, two previous studies explored a similar dust haze analysis, Marocco et al. (2014) for brown dwarfs and Bonnefoy et al. (2015) for directly imaged exoplanets. Marocco et al. (2014), Bonnefoy et al. (2015), and this work are all motivated by the success of the interstellar reddening law in de-reddening unusually red L dwarf spectra and aim to explain the observed reddening by introducing a layer of small dust grains in the

upper atmospheres. Despite the similar ideas and concepts, the method we describe here is distinct from those previous studies as described in §4 and §6.3.

The sample of L dwarfs studied in this analysis is presented in §2. In §3, we present our method of using spectral observations to estimate the reddening. We explain our dust haze model in detail in §4, and model fitting method in §5. Finally, we present our results in §6 and conclusion in §7.

2. Sample and Spectral Observations

In order to study the observed reddening, we compiled a sample of low-resolution NIR spectra of 23 L dwarfs with low gravity features in the optical (Cruz et al. 2009) and 23 red field L dwarfs (Kirkpatrick et al. 2010).

Our red field objects have spectral features indicative of field gravity with $J - K$ colors redder than the spectral standards (Kirkpatrick et al. 2010). This definition of ‘red’ is specific to the purpose of this analysis. For example, Faherty et al. (2013) defined ‘red’ as having a redder $J - K$ color than the mean $J - K$ of normal objects in the spectral type as opposed to comparing to the spectral standard. Therefore, red objects in our sample may be different from objects that are defined red by Faherty et al. (2013) or other papers. The objects in our sample are listed in Table 1.

Our sample includes 18 new spectra of red L dwarfs obtained with the SpeX spectrograph on the Infrared Telescope Facility (IRTF) (Rayner et al. 2003). Observations were obtained over 28 nights during 2003–2011. The targets and observation dates are listed in Table 1. All objects were observed in clear and dry conditions. The targets were observed dithered pairs (ABBA) to enable pair-wise subtraction. We used the 0.5" slit and prism-dispersed mode to obtain $\lambda/\Delta\lambda \approx 120$ spectra covering 0.7–2.5 μm . The data were reduced using the SpeXtool package (Cushing et al. 2004), nearby A0 V stars were observed for flux calibration and telluric correction (Vacca et al. 2003), and internal flat field and Ar arc lamp exposures were obtained for pixel response and wavelength calibration.

3. Estimating the Observed Reddening

In order to estimate the observed reddening, we compared red L dwarfs (including young and field) to the field spectral standards. The observed reddening was obtained by dividing the spectrum of the field standard by the spectrum of the red L dwarf. The top panel of Figure 1 shows spectra of a red L dwarf and a spectral standard, illustrating the

redder spectral slope of the red object. The bottom pane is the ratio of the two spectra and visualizes the estimated observed reddening of the red object. The small-scale features seen in the observed reddening are due to gravity-sensitive spectral features such as FeH, VO, and the triangular-shaped H band (Kirkpatrick et al. 2006; Allers & Liu 2013). We assume these features are not caused by reddening, so we treat the overall shape of the observed reddening as a smooth curve.

4. Modeling the Observed Reddening

In this paper, we develop a prescription for a hypothesized dust haze of small particles in the atmospheres of the so-called ‘red’ L dwarfs to explain the observed reddening in their spectral energy distributions (SEDs). In order to model the observed reddening, we used Mie theory to calculate the ‘raw’ extinction coefficients due to forsterite grains. Then we averaged the raw extinction coefficients over various particle size distributions to calculate the ‘effective’ extinction coefficients and to generate a model grid to compare with the observed reddening.

4.1. Dust Haze Prescription

In Figure 2, we show an illustration of the proposed dust haze in the upper atmospheres of red L dwarfs. Our model prescribes that the dust haze must be high in the atmospheres so that it is too cool (since the temperature decreases as the altitude increases) to radiate significantly in the NIR. The prescribed dust haze lies above the main cloud deck, so the dust grains in the haze affect the emergent spectra. Our prescription does not have thickness or height, therefore we are not constraining the position or dimensions of the dust haze any further than lying above the main cloud deck.

The dust haze grains were modeled by forsterite grains. As shown by Lodders and Fegley (2006), forsterite (Mg_2SiO_4) is thought to exist in L dwarf atmospheres among other dust species such as corundum (Al_2O_3), enstatite (MgSiO_3), and iron. Corundum condenses at higher temperatures in the atmospheres of late M dwarfs. Liquid iron and silicates condense in early L dwarfs between 1600 – 1840 K. Since iron grains form deeper in the atmosphere, the dust is most likely silicate. The silicate grains in the L dwarf atmospheres are thought to be a mixture of forsterite and enstatite. Since the extinction curves of forsterite and enstatite have similar shapes, forsterite was used in our analysis.

Extinction is the sum of absorption and scattering, and is the fraction of incoming

light that gets affected by interactions with particles. Reddening is a type of extinction, which occurs when extinction is more effective at shorter (bluer) wavelengths than at longer (redder) wavelengths, and has the effect of making the spectral slope redder. We used Mie theory to model the reddening effect of the proposed dust haze on the emergent spectra of red L dwarfs. Mie theory applies when the scattering particle is spherical and its size is similar to the wavelength of the scattered light, which is appropriate for sub-micron size grains in the NIR. For larger particles, Mie scattering is independent of wavelength while for smaller particles, it is wavelength dependent. Mie scattering reduces to strongly wavelength dependent Rayleigh scattering when particle sizes are much smaller than wavelength. We employed a Mie code, described in Toon and Ackerman (1981), and the refractive indices of forsterite (G. Sloan, pers. comm.) to compute the ‘raw’ extinction coefficients, $Q_{\text{ext}}(r, \lambda)$, for particles of radii between 0.01 and 10 μm .

4.2. Particle Size Distributions

In order to calculate effective extinction coefficients from the ‘raw’ extinction coefficients directly computed from the Mie code, we need to choose a particle size distribution $n(r)$. We considered three different particle size distributions commonly used to model grains, clouds and hazes in various settings: power law, Gaussian, and Hansen distributions. Figure 3, compares the shape of the three distributions. We describe the motivation to use these particle size distributions and results below.

We considered a power law particle size distribution $n(r) \propto r^p$ with $p = -3$ and particle radius r ranging between 0.01 – 10 μm to model theoretical extinction due to the proposed small dust grains. Power law particle size distributions with $p \approx -3.5$ are typically used to characterize interstellar dust and grains in the circumstellar disks around young brown dwarfs (Mathis et al. 1977; Draine 2006; Luhman et al. 2005; Broekhoven-Fiene et al. 2014). Figure 3 shows two different power law particle size distributions with $p = -3$ and -3.5 .

We also considered a Gaussian particle size distribution $n(r) = \frac{1}{\sqrt{2\pi}\sigma} e^{-\frac{(r-\mu)^2}{2\sigma^2}}$ with the mean radius $\mu = 0.5\mu\text{m}$ and a width $\sqrt{2}\sigma = 0.1 \times \mu$. This particle size distribution is adopted from Marocco et al. (2014), who de-reddened ULAS J222711–004547 using corundum and enstatite, and other red L dwarfs using corundum with Gaussian particle size distributions and found $\mu \sim 0.5\mu\text{m}$.

We also considered the Hansen particle size distribution, which is a variation of the

gamma distribution and is expressed as follows.

$$n(r) = r^{\frac{1-3b}{b}} e^{-\frac{r}{ab}} \quad (1)$$

where a is the mean effective radius and b is the effective variance. Following Hansen (1971), a and b are defined as

$$a = \frac{\int_0^\infty r \pi r^2 n(r) dr}{\int_0^\infty \pi r^2 n(r) dr} \quad (2)$$

$$b = \frac{\int_0^\infty (r - a)^2 \pi r^2 n(r) dr}{a^2 \int_0^\infty \pi r^2 n(r) dr} \quad (3)$$

respectively.

The Hansen particle size distribution successfully reproduces the observed particle size distributions of different types of water clouds in Earth’s atmosphere (fair weather cumulus, altostratus, and stratus clouds) as shown in Figure 1 of Hansen (1971). Figure 3 shows two Hansen particle size distributions with the mean effective radius $a = 0.2 \mu\text{m}$ for effective variances $b = 0.1$ and 0.5 . The Hansen particle size distribution with a large variance (dashed green, $b = 0.5$) is similar to power law particle size distributions in the regime of small particle size ($\lesssim 0.1 \mu\text{m}$).

4.3. Computing Modeled Extinction Curves and Comparing to Observations

In order to account for a range of particle sizes and to smooth over the small-scale interference patterns in forsterite extinction coefficients, we computed effective extinction coefficients by averaging the raw extinction coefficients over a particle size distribution. Effective extinction coefficients are defined as

$$Q_{\text{ext}}(\lambda) = \frac{\int_{r_{\text{min}}}^{r_{\text{max}}} \pi r^2 Q_{\text{ext}}(r, \lambda) n(r) dr}{\int_{r_{\text{min}}}^{r_{\text{max}}} \pi r^2 n(r) dr} \quad (4)$$

where $n(r)dr$ is the number of particles per unit volume with radius between r and $r + dr$. The integration limits we employed are $0.01\text{--}10 \mu\text{m}$. Particles smaller than this range would be too small (a few atoms) to scatter light and particles that exceed $10 \mu\text{m}$ tend to be grey at all wavelengths (i.e. the extinction they cause will be independent of wavelength).

In order to compare the observed reddening to the modeled extinction, we assume that the observed flux, I , from a red L dwarf can be modeled as

$$I(\lambda) = f I_0(\lambda) e^{-\tau(\lambda)} \quad (5)$$

where $I_0(\lambda)$ is the flux of the field standard L dwarf, f is a scaling factor, and $\tau(\lambda)$ is the optical depth of the dust haze in the red L dwarf atmosphere, assuming the red L dwarf can be described by the field L dwarf surrounded by the dust haze as in Figure 2. The scaling factor f is determined by the distances and sizes of the objects.

$$f = \frac{d_0^2 R^2}{d^2 R_0^2} \quad (6)$$

where d_0 and d are the distances to the field and the red L dwarfs, and R and R_0 are the radii of the red and the field L dwarfs, respectively.

Solving Equation 1 for the optical depth we get

$$\tau(\lambda) = \ln f + \ln \frac{I_0(\lambda)}{I(\lambda)}. \quad (7)$$

The optical depth $\tau(\lambda)$ is related to the Mie extinction coefficient $Q_{\text{ext}}(\lambda)$ as

$$\tau(\lambda) = N\pi a^2 Q_{\text{ext}}(\lambda) \quad (8)$$

where N is the column density of the haze layer and a is the effective radius of the scattering grains which we assume are composed of forsterite. $Q_{\text{ext}}(\lambda)$ is the wavelength dependent forsterite grain extinction coefficient which we calculated using the Mie code (Toon and Ackerman 1981). We averaged the forsterite coefficients over a particle size distribution $n(r)$ as described in Equation 4.

Combining Equations 7 and 8, we get

$$\ln \frac{I_0(\lambda)}{I(\lambda)} = N\pi a^2 Q_{\text{ext}}(\lambda) + C \quad (9)$$

where N , a , and $Q_{\text{ext}}(\lambda)$ are the column density of the dust haze, the mean effective radius found from the particle size distribution $n(r)$, and the effective forsterite extinction coefficients of small grains from Equation 4. The constant term C accounts for the scaling factor f and any differences in grey atmospheric opacity between the L dwarfs. Since the reddening we observe is wavelength dependent, we relegate any grey component to the C term. C is independent of wavelength because $Q_{\text{ext}}(\lambda)$ approaches a constant for $a \gg \lambda$. The RHS of Equation 9 is the modeled extinction and the LHS is the observed reddening. As explained later in §5, we used MCMC methods to constrain the parameters in the modeled extinction (N , a) that best reproduce the observed reddening.

4.3.1. Evaluation of Particle Size Distributions and Creating a Model Grid

Figure 4 shows model fits to the observed extinction using the three different particle size distributions. The top panel shows the observed reddening (black, same as the bottom

panel in Figure 1), theoretical extinction curves using the Hansen, power law, and Gaussian particle size distributions. χ^2 value and the degrees of freedom for each fit are reported in the legend. The bottom panel shows the residual between the observed reddening and the theoretical extinction curve as a percentage of the observed flux. Figure 4 demonstrates that all three modeled extinction curves fit the observed reddening reasonably. The Hansen and power law particle size distributions reproduce the smooth shape of the observed reddening, while the Gaussian particle size distribution results in a less smooth extinction curve.

For the remainder of our analysis, we adopt the Hansen particle size distribution because of the favorable behavior shown in Figure 4, the fact that it reflects the microphysics and structure of Earth’s clouds, and because it has various helpful properties that are useful for algebraic manipulation (Hansen 1971).

In Figure 5, we show our model grid of forsterite extinction coefficients for various Hansen particle size distributions. The effective forsterite extinction curves for small mean particle sizes ($a \leq 0.4 \mu\text{m}$) more closely resemble the observed reddening than those with a larger mean particle size. For these small mean particle sizes, extinction coefficients are wavelength dependent and resemble the curved shapes of the observed reddening (Figure 1). For particles larger than $0.4 \mu\text{m}$, extinction coefficients are less wavelength dependent and the resulting extinction shapes are flat (‘grey’), which do not fit the observed reddening. The curves for $a = 1.0 \mu\text{m}$ are shown as representatives of the curves with $a > 0.4 \mu\text{m}$.

The range of effective variance b was determined based on the shape of the Hansen particle size distribution. Small effective variances ($b < 0.1$) result in a particle size distribution concentrated at the mean effective radius, and large effective variances ($b > 1$) make the particle size distribution wide and resemble a power law particle size distribution. Thus, we decided to use Hansen particle distribution with a parameter grid of mean effective radius a between 0.05 and $0.4 \mu\text{m}$, and effective variance b between 0.1 and 1.0 as priors for the rest of our analysis.

5. Methods: Fitting the Models to the Observed Reddening

We use Markov-chain Monte Carlo (MCMC) fitting to estimate the best-fit parameters and their uncertainties. MCMC is a Bayesian inference method which provides a sampling approximation of the posterior probability distribution function (PDF). An MCMC run produces a chain of positions in parameter space, and a histogram of these positions provides the approximation of the posterior PDF. MCMC allows for more in-depth probabilistic data analysis than χ^2 minimization, for example, it efficiently approximates the full posterior

PDF, which in turn provides uncertainties on and illustrates covariances between model parameters.

The Goodman-Weare (G-W) algorithm improves upon the Metropolis-Hastings (M-H) algorithm by changing the method for choosing trial positions (Goodman and Weare 2010). The G-W algorithm deploys an ensemble of chains, known as “walkers”, instead of a single chain. The trial position for each walker is chosen from the ensemble’s location in parameter space, with some probability for choosing a position outside the occupied region. This method does not require hand-tuning the step size for each parameter, and the selection of trial positions can be parallelized. The G-W algorithm more efficient than the M-H algorithm in both human working hours and computation time. (Goodman and Weare 2010; Foreman-Mackey et al. 2013)

We use the open-source python implementation of the G-W algorithm, *emcee* (Foreman-Mackey et al. 2013), to fit the observed reddening with our model grid described in §4.3. The modeled extinction curves are parameterized by the mean particle size a and effective variance b for the Hansen distribution and the column density N of forsterite grains. We assume an unnormalized flat prior probability distribution for each parameter. The effective extinction coefficients are linearly interpolated and the modeled extinction at each wavelength point is calculated as Equation 9.

We also model the vertical offset between the observed reddening and the extinction curve with a constant C , and include a tolerance parameter s . The tolerance s estimates the uncertainty in the model as a single value across the extinction curve; it accounts for the fact that the photon-noise uncertainties are smaller than the typical difference between each observed reddening point and the corresponding point on the extinction curve. If we denote observed reddening points as $r = \{r_i\}$ and the corresponding uncertainties as $\sigma_0 = \{\sigma_{0,i}\}$, we compute the natural logarithm of the likelihood function as

$$\ln \mathcal{L}(r|a, b, N, C, s, \sigma_0) = -\frac{1}{2} \sum_i \left[\frac{(r_i - (N\pi a^2 Q_i^2 + C))^2}{(\sigma_{0,i}^2 + s^2)} + \ln(2\pi (\sigma_{0,i}^2 + s^2)) \right] \quad (10)$$

The natural logarithm of the posterior PDF is given by

$$\ln(\text{PDF})(a, b, N, C, s|r, \sigma_0) = \ln \mathcal{L}(r|a, b, N, C, s, \sigma_0) + \ln \mathcal{P}(a, b, N, C, s, \sigma_0) \quad (11)$$

We assume an unnormalized flat prior on each parameter, so $\mathcal{P}(a, b, N, C, s, \sigma_0) = 1$ and $\ln \mathcal{P}(a, b, N, C, s, \sigma_0) = 0$.

We pass a function for $\ln(\text{PDF})$ to *emcee*, which uses that function to determine acceptance of each step in parameter space. We typically use 100 walkers. After we iterate for 200 steps to generate a new set of initial positions for the walkers, we reset the walkers and

restart from the new initial positions. We iterate for 2000 steps after a burn-in period of 200 steps.

6. Results and Discussion

6.1. Fitting Dust Haze Parameters

We used the MCMC method described in §5 to fit dust haze extinction models to the observed reddening curves for each object and constrain the physical properties of the proposed dust haze. We plot the 1D and 2D marginalized posterior PDFs for all parameters in Figure Set 6. Models corresponding to 100 randomly-drawn parameter sets from the posterior PDF are shown with the data in Figure Set 7. The constrained properties of the dust haze include mean effective radius, effective variance of the Hansen distribution (§4.2), and column density of the dust haze.

In Figure Set 6, we show the posterior distributions for each parameter. Each figure has 1-D distributions for the parameters and 2-D contours for each combination of parameters. Gaussian-like 1-D distributions and round 2-D contours indicate no covariances. Quantiles (16, 50, 84 %) are shown with dashed lines and are used to report the uncertainties on the parameter fits. In many objects, the PDFs for the mean effective radius a , column density N , tolerance parameter $\log s$, and vertical offset constant C have clear peaks and therefore are well constrained. The variance b , on the other hand, is not well constrained in most objects.

The column density values N are comparable to the value of typical brown dwarf atmospheres ($\sim 10^8 \text{ cm}^{-2}$), which indicates that our results are reasonably realistic. However, there is a correlation between parameters a and N as seen in the 2-D contours. The relationship between a and N is shown in Equation 9. In order to compute the optical depth, we multiply the column density N , scattering cross section πa^2 , and effective extinction coefficient $Q_{\text{ext}}(\lambda)$. The effective extinction curves are similar over a small range of grain radii, so we are constraining the product Na^2 . Therefore, a^2 and N are inversely proportional and this relationship appears in the posterior distributions.

In Figure Set 7, we show the resulting model fits to the observed reddening. The black line is the observed reddening (§3) and the green lines are 100 models randomly drawn from the posterior distributions. The models reproduce the overall shape of the observed reddening.

In Figure Set 8, we compare a de-reddened spectrum of a red L dwarf, the spectrum

of the field standard L dwarf, and the original red L dwarf spectrum. The de-reddened spectrum is the spectrum of a red L dwarf corrected by the best-fit forsterite extinction curve determined by the MCMC analysis. χ^2 values between the red and standard spectra, and between the de-reddened and standard spectra are reported. The χ^2 values are used simply to quantitatively demonstrate that the de-reddened spectrum is a better fit to the standard spectrum than the original red L dwarf spectrum. The tolerance parameter s is not included in the calculation because it is not necessary for this purpose. In all cases the de-reddened spectrum fits the standard spectrum better than the original red L dwarf spectrum, as reflected by the significant improvement of χ^2 value after the de-reddening.

In Figures 9 and 9.2, we show an example of the de-reddened spectra (Figure Set 8) and model fits (Figure Set 7) for each spectral type. In all spectral types, the de-reddened spectra looks much closer to the standard spectra than the original red L dwarf spectra. These results show that the submicron-sized dust haze prescription can successfully account for the red SED and $J - K_s$ colors of L dwarfs.

In Figure 10, we show improvement in χ^2 due to the proposed dust haze prescription. The ratio of χ^2 before de-reddening to χ^2 after de-reddening is plotted against $\Delta(J - K_s)$ color, which is the difference in $J - K_s$ color between the red L dwarf and the field standard L dwarf. We use $\Delta(J - K_s)$ because we compare the spectra of red L dwarfs to the standards to isolate the observed reddening. The value of χ^2 is improved for all objects, which shows that the de-reddened spectra fit the field standards better, and in most cases substantially better ($> 10\times$), than the original red L dwarf spectra.

6.2. Correlation with Gravity

It has been widely noted that low-gravity L dwarfs have redder NIR spectral energy distributions compared to the field-gravity spectral standards. A discussion of how clouds behave differently at low and moderate gravity is given in Marley et al. (2012). In addition to the cloud height differences discussed by Marley et al. (2012), one might expect to see a correlation between dust haze properties and low-gravity spectral features. We hypothesized that the proposed dust haze might dissipate over time due to grain growth by condensation. Large condensed particles are expected to fall out of the dust haze as a result of the sedimentation rate exceeding the remixing rate by eddy turbulence (Marley et al. 1999). Reduced convective velocities and perhaps less vigorous gravity wave excitation with age could also contribute to more efficient dust settling. Thus, young, low gravity L dwarfs might have optically thicker dust hazes which may explain their red NIR colors. The proposed dust haze could also explain the reddening within field L dwarfs and the properties of the dust

haze might be correlated with age.

In Figures 11 and 12, we show scatter plots of mean effective radius a and column density N versus $\Delta(J - K)$ color, respectively. Green symbols denote low-gravity objects and magenta denote field-gravity. Circles denote objects with PDFs with strong constraints, while squares and diamonds denote objects with weak constraints for some of the parameters. There are visually noticeable differences between the distributions of the low-gravity and field-gravity objects in both Figure 11 and Figure 12. In Figure 11, we show that there is no correlation between mean effective radius a and $\Delta(J - K)$ color for the low-gravity objects, while the distribution of the field-gravity objects show a correlation. In Figure 12, the distribution of the low-gravity objects span a wider range of column densities, while the field-gravity objects tend to have lower column densities. Even though there are visible differences between the distributions of the low-gravity and field-gravity objects, the two distributions partially overlap and the correlations are not strong.

In order to quantitatively determine if the distributions of the low-gravity objects and the field-gravity objects are indeed different, we performed a two-dimensional K-S test on the two distributions in both Figure 11 and Figure 12. The probability of the two distributions in Figure 11 drawn from the same parent distribution is $2.32 \cdot 10^{-4}$, and the probability of the two distributions in Figure 12 drawn from the same parent distribution is $5.11 \cdot 10^{-6}$. These results show that the low-gravity and the field-gravity objects are most likely drawn from different distributions.

The lack of strong correlations between the dust haze properties and gravity might be due to a model grid not spanning a wide enough range of effective variance, b . We consider $0.1 < b < 1.0$ because Hansen particle size distributions for large b look like a power law size distribution (Figure 3; Equation 1). This makes the results for these objects somewhat unreliable. In most of those objects, b tends to be close to the upper limit and therefore is not well constrained (Figure Set 6).

Further, our initial assumptions about low-gravity and field L dwarfs may be unrealistic. We assumed that low-gravity and field L dwarfs with the same base spectral type (e.g. L2 and L2 γ) have the same effective temperatures and the low-gravity L dwarf has the hypothetical dust haze of small grains in the upper atmosphere. However, recent evidence suggests that low-gravity L dwarfs do not necessarily share the same physical properties with field L dwarfs just because they share the same base spectral type (Luhman 2012; Filippazzo et al. 2015). Young, low gravity L dwarfs might have cooler effective temperatures than field L dwarfs in the same spectral classification (Faherty et al. 2013). This suggests that an earlier type standard would be a better comparison. We could be comparing objects with different effective temperatures and thus, not setting accurate estimates of the dust haze properties.

Since the overall shape of a spectrum is very sensitive to the effective temperature, comparing objects with the same effective temperatures might be more useful for future analysis.

Finally, the overlapping distributions of a and N may indicate that the dust hazes of low-gravity and red field L dwarfs are not different from one another. It might be the case that gravity does not play a major role in determining the properties of the dust haze and the same distribution of dust haze properties exist in both low-gravity and red field L dwarfs. Some red field L dwarfs might have a dust haze for reasons other than gravity, such as differing rotation rates, composition, or evolutionary history.

6.3. Comparison to Marocco et al. (2014)

Independently, Marocco et al. (2014) (hereafter, M14) present results from a similar analysis. Bonnefoy et al. (2015) closely followed the approach of Marocco et al. (2014) so we do not consider it further here. Like us, they are motivated by the utility of the interstellar extinction law in de-reddening red L dwarf spectra, use Mie theory to characterize a high-altitude population of sub-micron dust grains, isolate the observed reddening by comparing red L dwarf spectra to spectral standards.

However, M14 consider corundum (Al_2O_3), enstatite (MgSiO_3), and iron while we use forsterite (Mg_2SiO_4). We use forsterite as a test dust particle because extinction curves for forsterite, enstatite –both of which are silicates– and corundum all behave similarly in the near infrared. We use silicate instead of iron because silicate grains form higher in the atmosphere than iron. Actual dust grains in the brown dwarfs atmospheres are most likely a mixture of these species.

Our model includes more parameters than M14. They have two parameters: characteristic grain radius r and normalization of the extinction curve at $2.20 \mu\text{m}$ while our model includes mean effective grain radius a , effective grain size variance b , column density N , vertical offset C , and tolerance factor s as described in §4. The N and C parameters account for normalization as shown in Equation 9. M14 perform χ^2 minimization to select the best fit parameters and therefore do not have uncertainties, while we use MCMC to determine best fit parameters and their uncertainties.

The range of the characteristic grain radius M14 found for corundum and enstatite are slightly larger than what we found. They obtained $r = 0.4 - 0.6 \mu\text{m}$ for corundum and enstatite, while our results for the mean effective radius for forsterite are generally smaller ($0.15 - 0.35 \mu\text{m}$). Their results for the maximum radius of iron are $0.15 - 0.3 \mu\text{m}$, closer to the values we found for forsterite grains.

M14 applied their method to five red L dwarfs, and we applied our method to 46 red L dwarfs including low-gravity and field-gravity objects. They used objects with later spectral types (L5 – L7), so there is only one common object between their sample and ours. 2MASS 0355+1133 is used in both studies but compared to different spectral standards. M14 used SDSS J0835+1953 as the L5 standard while we used 2MASS 1507-1627. They found the characteristic grain radius for 2MASS 0355+1133 to be $0.4 \mu\text{m}$ and we found the mean effective radius to be $0.3^{+0.03}_{-0.02} \mu\text{m}$.

Regardless of the different methods, these two studies show similar results. The reproducibility of the results demonstrates the viability of sub-micron size dust grains, and warrants further study and inclusion of small dust grains in future atmosphere models.

7. Conclusion and Summary

The success of the interstellar reddening law in de-reddening L dwarf spectra led us to investigate the possibility of a population of small submicron-sized dust grains in red L dwarf atmospheres that can possibly explain their red NIR colors.

In order to isolate and characterize the reddening, we compare spectra of red L dwarfs to field spectral standards. The observed reddening is treated as smooth power-law shaped curves. We use Mie theory to model the dust haze of small particles with theoretical extinction curves.

We use a Markov-Chain Monte Carlo algorithm to fit the theoretical extinction curves to the observed reddening in order to find the best-fit values and uncertainties for the properties of the dust haze. We apply this method to 23 L dwarfs with low-gravity spectral features and 23 field L dwarfs with redder $J - K$ colors than the spectral standards. We find that small forsterite grains ($< 0.5 \mu\text{m}$) reproduce the observed reddening. There are differences in grain properties between low-gravity and field L dwarfs, which indicates that dust haze properties may be correlated with surface gravity. The best-fit column densities of forsterite grains are reasonable compared to typical brown dwarf atmospheres. These results suggest that a dust haze of small particles with a Hansen particle size distribution can account for the observed red NIR spectral energy distributions of brown dwarfs. However, to rigorously explore this hypothesis other particle species and particle size distributions should be explored as well.

This work is a proof of concept and it provides a strong motivation for including small dust grains in future atmosphere models of brown dwarfs. Future work on the role of small grains in brown dwarf atmospheres will include other grain species such as corundum and enstatite. The dust haze analysis can be applied to other studies including variability in

brown dwarfs, exoplanet atmospheres, and the interstellar/intergalactic medium.

We thank our anonymous referee for thorough and helpful comments. This material is based upon work supported by the National Science Foundation under Grant No. AST-1313278. Support for this project was provided by a PSC-CUNY Award, jointly funded by The Professional Staff Congress and The City University of New York.

REFERENCES

- Ackerman, A. S., and Marley, M. S. 2001, *Astrophysical Journal*, 556, 872
- Allard, F., Hauschildt, P. H., Alexander, D. R., Tamanai, A., and Schweitzer, A. 2001, *Astrophysical Journal*, 556, 357
- Allers, K. N., Liu, M. C., Dupuy, T. J., and Cushing, M. C. 2010, *Astrophysical Journal*, 715, 561
- Allers, K. N. and Liu, M. C. 2013, *Astrophysical Journal*, 772, 79
- Bardalez Gagliuffi, D. C., Burgasser, A. J., Gelino, C. R., Looper, D. L., Nicholls, C. P., Schmidt, S. J., Cruz, K. L., West, A. A., Gizis, J. E., and Metchev, S. 2014, *Astrophysical Journal*, 794, 143
- Bonnefoy, M., Zurlo, A., Baudino, J. L., Lucas, P., Mesa, D., Maire, A.-L., Vigan, A., Galicher, R., Homeier, D., Marocco, F., Gratton, R., Chauvin, G., Allard, F., Desidera, S., Kasper, M., Moutou, C., Lagrange, A.-M., Baruffolo, A., Baudrand, J., Beuzit, J.-L., Boccaletti, A., Cantalloube, F., Carbillet, M., Charton, J., Claudi, R. U., Costille, A., Dohlen, K., Dominik, C., Fantinel, D., Feautrier, P., Feldt, M., Fusco, T., Gigan, P., Girard, J. H., Gluck, L., Gry, C., Henning, T., Janson, M., Langlois, M., Madec, F., Magnard, Y., Maurel, D., Mawet, D., Meyer, M. R., Milli, J., Moeller-Nilsson, O., Mouillet, D., Pavlov, A., Perret, D., Pujet, P., Quanz, S. P., Rochat, S., Rousset, G., Roux, A., Salasnich, B., Salter, G., Sauvage, J.-F., Schmid, H. M., Sevin, A., Soenke, C., Stadler, E., Turatto, M., Udry, S., Vakili, F., Wahhaj, Z., and Wildi, F. 2015arXiv151104082B
- Broekhoven-Fiene, H., Matthews, B., Duchene, G., Di Francesco, J., Scholz, Al., Chrysostomou, A., Jayawardhana, R. 2014, *Astrophysical Journal*, 789, 155

- Bouy, H, Brandner, W, Martn, E. L., Delfosse, X., Allard, F., and Basri, G. 2003, *Astronomical Journal*, 126, 1526
- Burgasser, A. J., and McElwain, M. W. *Astronomical Journal*, 131, 1007
- Burgasser, A. J. 2007, *Astrophysical Journal*, 659, 655
- Burgasser, A. J. 2008, *PhT*, 61, 70
- Burgasser, A. J., Liu, M. C., Ireland, M. J., Cruz, K. L., and Dupuy, T. J. 2008, *Astrophysical Journal*, 681, 579
- Burgasser, A. J., Cruz, K. L., Cushing, M. C., Gelino, C. R., Looper, D. L., Faherty, J. K., Kirkpatrick, J. D., and Reid, I. N. 2010 *Astrophysical Journal*, 710, 1142
- Burgasser, A. J., Simcoe, R. A., Bochanski, J. J., Saumon, D., Mamajek, E. E., Cushing, M. C., Marley, M. S., McMurtry, C., Pipher, J. L., and Forrest, W. J. 2010, *Astrophysical Journal*, 725, 1405
- Burgasser, A. J., Bardalez-Gagliuffi, D. C., and Gizis, J. E. 2011, *Astronomical Journal*, 141, 70
- Burrows, A., Hubbard, W. B., Lunine, J. I., and Liebert, J. *Reviews of Modern Physics*, 73, 719
- Cardelli, J. A., Clayton, G. C., and Mathis, J. S. 1989, *Astrophysical Journal*, 345, 245
- Chiu, K., Fan, X., Leggett, S. K., Golimowski, D. A., Zheng, W., Geballe, T. R., Schneider, D. P., and Brinkmann, J. 2006, *Astronomical Journal*, 131, 2722
- Cruz, K. L., Reid, I. N., Liebert, J., Kirkpatrick, J. D., and Lowrance, P. J. *Astronomical Journal*, 126, 2421
- Cruz, K. L., Burgasser, A. J., Reid, I. N., and Liebert, J. 2004, *Astrophysical Journal*, 604, 61
- Cruz, K. L., Reid, I. N., Kirkpatrick, J. D., Burgasser, A. J., Liebert, J., Solomon, A. R., Schmidt, S. J., Allen, P. R., Hawley, S. L., and Covey, K. R. 2007, *Astronomical Journal*, 133, 439
- Cruz, K. L., Kirkpatrick, J. D., and Burgasser, A. J. 2009, *Astronomical Journal*, 137, 3345
- Cushing, M. C., Vacca, W. D., & Rayner, J. T. 2004, *Publications of the Astronomical Society of the Pacific*, 116, 362

- Cushing, M. C., Roellig, T. L., Marley, M. S., Saumon, D., Leggett, S. K., Kirkpatrick, J. D., Wilson, J. C., Sloan, G. C., Mainzer, A. K., Van Cleve, J. E., and Houck, J. R. 2006, *Astrophysical Journal*, 648, 614
- Cushing, M. C., Marley, M. S., Saumon, D., Kelly, B. C., Vacca, W. D., Rayner, J. T., Freedman, R. S., Lodders, K., and Roelling, T. L. 2008, *Astrophysical Journal*, 678, 1372
- Dahn, C. C., Harris, H. C., Vrba, F. J., Guetter, H. H., Canzian, B., Henden, A. A., Levine, S. E., Luginbuhl, C. B., Monet, A. K. B., Monet, D. G., Pier, J. R., Stone, R. C., Walker, R. L., Burgasser, A. J., Gizis, J. E., Kirkpatrick, J. D., Liebert, J., and Reid, I. N. 2002, *Astronomical Journal*, 124, 1170
- Delfosse, X., Tinney, C. G., Forveille, T., Epchtein, N., Bertin, E., Borsenberger, J., Copet, E., de Batz, B., Fouque, P., Kimeswenger, S., Le Bertre, T., Lacombe, F., Rouan, D., and Tiphene, D. 1997, *Astronomy & Astrophysics*, 327, 25
- Draine, B. T. 2006, *Astrophysical Journal*, 636, 1114
- Faherty, J. K., Burgasser, A. J., Cruz, K. L., Shara, M., Walter, F. M., and Gelino, C. R. 2009, *Astrophysical Journal*, 137, 1
- Faherty, J. K., Rice, E. L., Crus, K. L., Mamajek, E. E., and Nunez, A. 2013, *Astronomical Journal*, 145, 2
- Fan, X., Knapp, G. R., Strauss, M. A., Gunn, J. E., Lupton, R. H., Ivezić, Z., Rockosi, C. M., Yanny, B., Kent, S., Schneider, D. P., Kirkpatrick, J. D., Annis, J., Bastian, S., Berman, E., Brinkmann, J., Csabai, I., Federwitz, G. R., Fukugita, M., Gurbani, V. K., Hennessy, G. S., Hindsley, R. B., Ichikawa, T., Lamb, D. Q., Lindenmeyer, C., Mantsch, P. M., McKay, T. A., Munn, J. A., Nash, T., Okamura, S., Pauls, A. G., Pier, J. R., Rechenmacher, R., Rivetta, C. H., Sergey, G., Stoughton, C., Szalay, A. S., Szokoly, G. P., Tucker, D. L., York, D. G., SDSS Collaboration, 2000, *Astronomical Journal*, 119, 928
- Filippazzo, J. C., Rice, E. L., Faherty, J. K., Cruz, K. L., Van Gordon, M. M., and Looper, D. L. 2015, [arXiv:1508.01767](https://arxiv.org/abs/1508.01767)
- Fitzpatrick, E. L., 1999, *Publications of the Astronomical Society of the Pacific*, 111, 63
- Ford, E. B. 2005, *Astronomical Journal*, 129, 1726
- Foreman-Mackey, D. et al. 2013, *Publications of the Astronomical Society of the Pacific*, 125, 306

- Gagne, J., Lafreniere, D., Doyon, R., Artigau, E., Malo, L., Robert, J., and Nadeau, D. 2014, *Astrophysical Journal*, 792, 17
- Gagne, J., Faherty, J. K., Cruz, K. L., Lafreniere, D., Doyon, R., Malo, L., Burgasser, A. J., Naud, M.-E., Artigau, E., Bouchard, S., Gizis, J. E., Albert, L. 2015, 219, 33
- Geballe, T. R., Knapp, G. R., Leggett, S. K., Fan, X., Golimowski, D. A., Anderson, S., Brinkmann, J., Csabai, I., Gunn, J. E., Hawley, S. L., Hennessy, G., Henry, T. J., Hill, G. J., Hindsley, R. B., Ivezić, Z., Lupton, R. H., McDaniel, A., Munn, J. A., Narayanan, V. K., Peng, E., Pier, J. R., Rockosi, C. M., Schneider, D. P., Smith, J. Allyn, Strauss, M. A., Tsvetanov, Z. I., Uomoto, A., York, D. G., Zheng, W. 2002, *Astrophysical Journal*, 564, 466
- Gizis, J. E., Monet, D. G., Reid, I. N., Kirkpatrick, J. D., Liebert, J., and Williams, R. J. 2000, *Astronomical Journal*, 120, 1085
- Gizis, J. E., Kirkpatrick, J. D., and Wilson, J. C. 2001, *Astronomical Journal*, 121, 2185
- Gizis, J. E., Reid, I. N., Knapp, G. R., Liebert, J., Kirkpatrick, J. D., Koerner, D. W., and Burgasser, A. J. 2003, *Astronomical Journal*, 125, 3302
- Goldman, B. et al. 1999, *Astronomy & Astrophysics*, 351, 5
- Goodman, J. and Weare, J. 2010, *Comm. App. Math. Comp. Sci.*, 5, 65
- Hansen, James E. 1971, *Journal of the Atmospheric Sciences*, 28, 1400
- Kirkpatrick, J. D., Beichman, C. A., and Skrutskie, M. F. 1997, *Astrophysical Journal*, 476, 311
- Kirkpatrick, J. D., Reid, I. N., Liebert, J., Cutri, R. M., Nelson, B., Beichman, C. A., Dahn, C. C., Monet, D. G., Gizis, J. E., Skrutskie, M. F. 1999, *ApJ*, 519, 802
- Kirkpatrick, J. D., Reid, I. N., Liebert, J., Gizis, J. E., Burgasser, A. J., and Brown, M. E. 2000, *Astronomical Journal*, 120, 473
- Kirkpatrick, J. D., Barman, T. S., Burgasser, A. J., McGovern, M. R., McLean, I. S., Tinney, C. G., and Lowrance, P. J. 2006, *Astrophysical Journal*, 639, 1120
- Kirkpatrick, J. D., Cruz, K. L., Barman, T. S., Burgasser, A. J., Looper, D. L., Tinney, C. G., Gelino, C. R., Lowrance, P. J., Liebert, J., and Carpenter, J. M. 2008, *Astrophysical Journal*, 689, 1295

- Kirkpatrick, J. D., Looper, D. L., Burgasser, A. J., Schurr, S. D., Cutri, R. M., Cushing, M. C., Cruz, K. L., Sweet, A. C., Knapp, G. R., and Barman, T. S. 2010, *Astrophysical Journal*, 190, 100
- Knapp, G. R., Leggett, S. K., Fan, X., Marley, M. S., Geballe, T. R., Golimowski, D. A., Finkbeiner, D., Gunn, J. E., Hennawi, J., Ivezić, Z., Lupton, R. H., Schlegel, D. J., Strauss, M. A., Tsvetanov, Z. I., Chiu, K., Hoversten, E. A., Glazebrook, K., Zheng, W., Hendrickson, M., Williams, C. C., Uomoto, A., Vrba, F. J., Henden, A. A., Luginbuhl, C. B., Guetter, H. H., Munn, J. A., Canzian, B., Schneider, Donald P., Brinkmann, J. 2004, *Astronomical Journal*, 127, 3553
- Liu, M. C., Magnier, E. A., Deacon, N. R., Allers, K. N., Dupuy, T. J., Koston, M. C., Aller, K. M., Burgett, W. S., Chambers, K. C., and Draper, P. W. 2013, *Astrophysical Journal*, 777, 20
- Lodders, K. and Fegley, B., Jr. 2006, *Astrophysics Update 2*, Springer Praxis Books
- Looper, D. L., Kirkpatrick, J. D., Cutri, R. M., Barman, T., Burgasser, A. J., Cushing, M. C., Roellig, T., McGovern, M. R., McLean, I. S., Rice, E. L., Swift, B. J., and Schurr, S. D. 2008, *Astrophysical Journal*, 686, 528
- Looper, D. L., Mohanty, S., Bochanski, J. J., Burgasser, A. J., Mamajek, E. E., Herczeg, G. J., West, A. A., Faherty, J. K., Rayner, J., Pitts, M. A., and Kirkpatrick, J. D. 2010, *Astrophysical Journal*, 714, 45
- Luhman, K. L., D’Alessio, P., Calvet, N., Allen, L. E., Hartmann, L., Forrest, W. J., Watson, D. M., Luhman, K. L., Uchida, K. I., Green, J. D., Sargent, B., Najita, J., Sloan, G. C., Keller, L. D., and Herter, T. L. 2005, *Astrophysical Journal*, 620, 51
- Luhman, K. L. 2012, *Astronomy & Astrophysics*, 50, 65
- Marley, M. S., Gelino, C., Stephens, D., Lunine, J. I., & Freedman, R. 1999, *Astrophysical Journal*, 513, 879
- Marley, M. S., Saumon, D., Cushing, M. C., Ackerman, A. S., Fortney, J. J., Freedman, R. 2012, *Astrophysical Journal*, 754, 135
- Mathis, J. S., Rumpl, W., Nordsieck, K. H. 1977, *Astrophysical Journal*, 217, 425
- Marocco, F., Day-Jones, A. C., Lucas, P. W., Jones, H. R. A., Smart, R. L., Zhang, Z. H., Gomes, J. I., Burningham, B., Pinfield, D. J., Raddi, R., and Smith, L. 2014, *Monthly Notices of the Royal Astronomical Society*, 439, 372

- Rayner, J. T., Toomey, D. W., Onaka, P. M., Denault, A. J., Stahlberger, W. E., Vacca, W. D., Cushing, M. C., and Wang, S. 2003, *PASP*, 115, 362
- Reid, I. N., Kirkpatrick, J. D., Gizis, J. E., Dahn, C. C., Monet, D. G., Williams, R. J., Liebert, J., and Burgasser, A. J. 2000, *Astronomical Journal*, 119, 369
- Reid, I. N., Lewitus, E., Burgasser, A. J., and Cruz, K. L. 2006, *Astrophysical Journal*, 639, 1114
- Reid, I. N., Cruz, K. L., Kirkpatrick, J. D., Allen, P. R., Mungall, F., Liebert, J., Lowrance, P., and Sweet, A. 2008, *Astronomical Journal*, 136, 1290
- Ruiz, M. T., Leggett, S. K., and Allard, F. 1997, *Astrophysical Journal*, 491, 107
- Saumon, D. and Marley, M. S. 2008, *Astrophysical Journal*, 689, 1327
- Siegler, N., Close, L. M., Burgasser, A. J., Cruz, K. L., Marois, C., Macintosh, B., and Barman, T. 2007, *Astronomical Journal*, 133, 2320
- Toon, O. B. and Ackerman, T. P. 1981, *Appl. Optics*, 20, 20
- Vacca, W. D., Cushing, M. C., & Rayner, J. T. 2003, *Publications of the Astronomical Society of the Pacific*, 115, 389
- Wilson, J. C., Miller, N. A., Gizis, J. E., Skrutskie, M. F., Houck, J. R., Kirkpatrick, J. D., Burgasser, A. J., and Monet, D. G. 2003, *Proceedings of IAU Symposium*, 211, 197
- Zhang, Z. H., Pokorny, R. S., Jones, H. R. A., Pinfield, D. J., Chen, P. S., Han, Z., Chen, D., Glvez-Ortiz, M. C., and Burningham, B. 2009, *Astronomy and Astrophysics*, 497, 619

Fig. Set 6. Posterior distributions for MCMC parameters

Fig. Set 7. Model fits

Fig. Set 8. De-reddened spectra

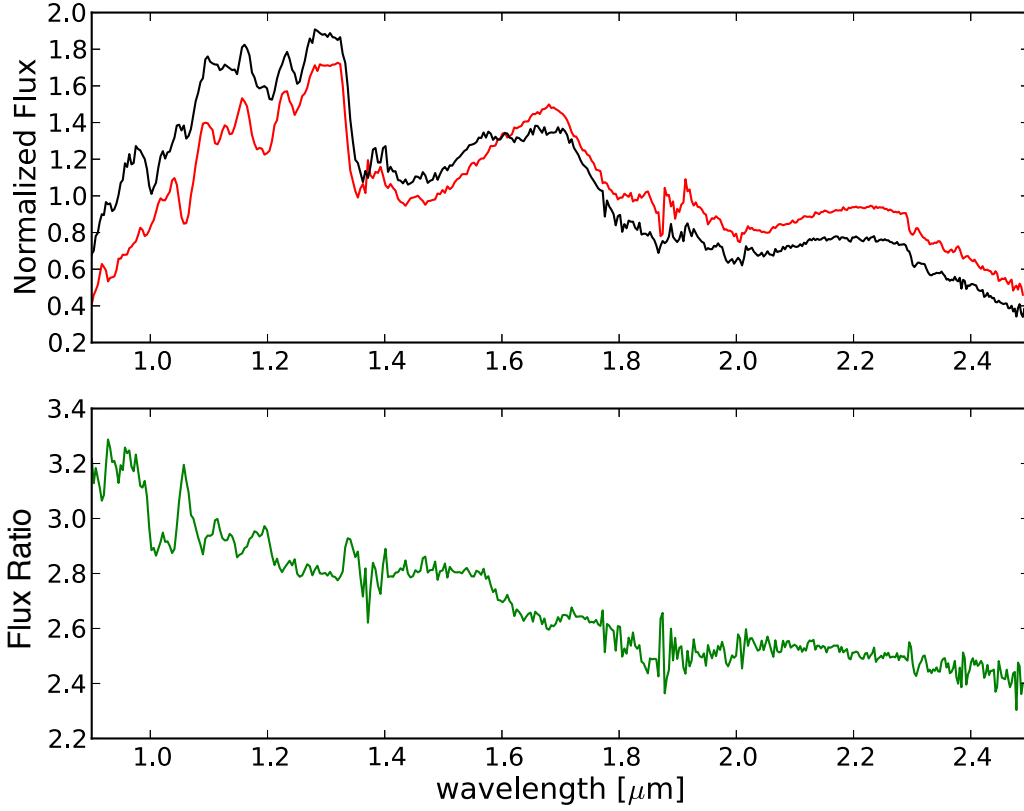


Fig. 1.— The top panel shows SpeX Prism spectra of a red L0 dwarf 2M 0141-4633 (red) and the L0 field standard 2M 0345+2540 (black). Each spectrum is normalized by the mean flux of the entire spectrum. The red object has excess flux longward of 1.5 μm . The bottom panel shows the observed reddening, which is the log of the flux ratio between 2M 0345+2540 and 2M 0141-4633.

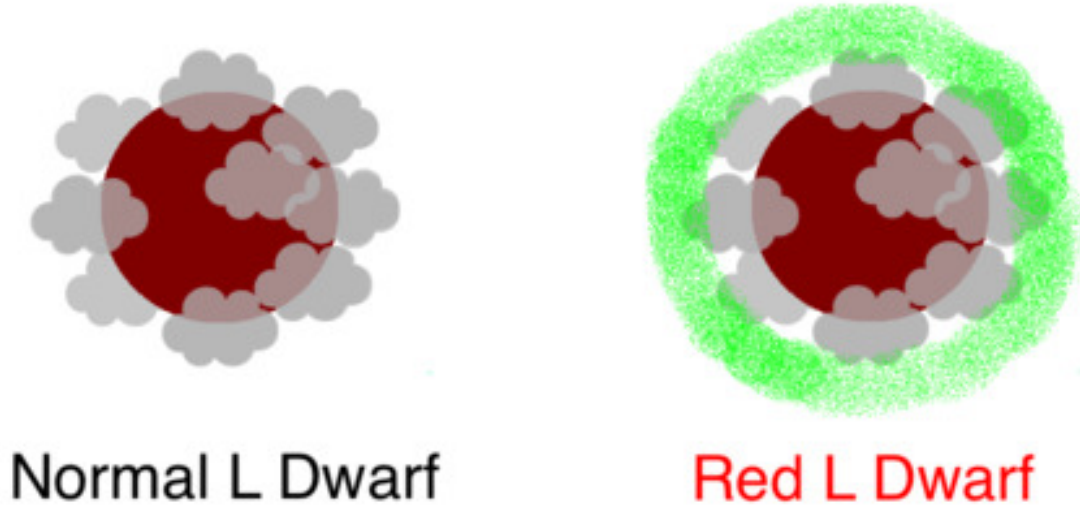


Fig. 2.— A conceptual representation of our dust haze model. The regular clouds of large particles ($\sim 10 \mu\text{m}$, grey cloud symbol) exist in both normal and red L dwarfs. An additional haze of small particles (green layer) is present in the red L dwarf atmosphere, which causes the observed reddening. We do not constrain the position or dimension of the haze any further than it lying above the main cloud deck.

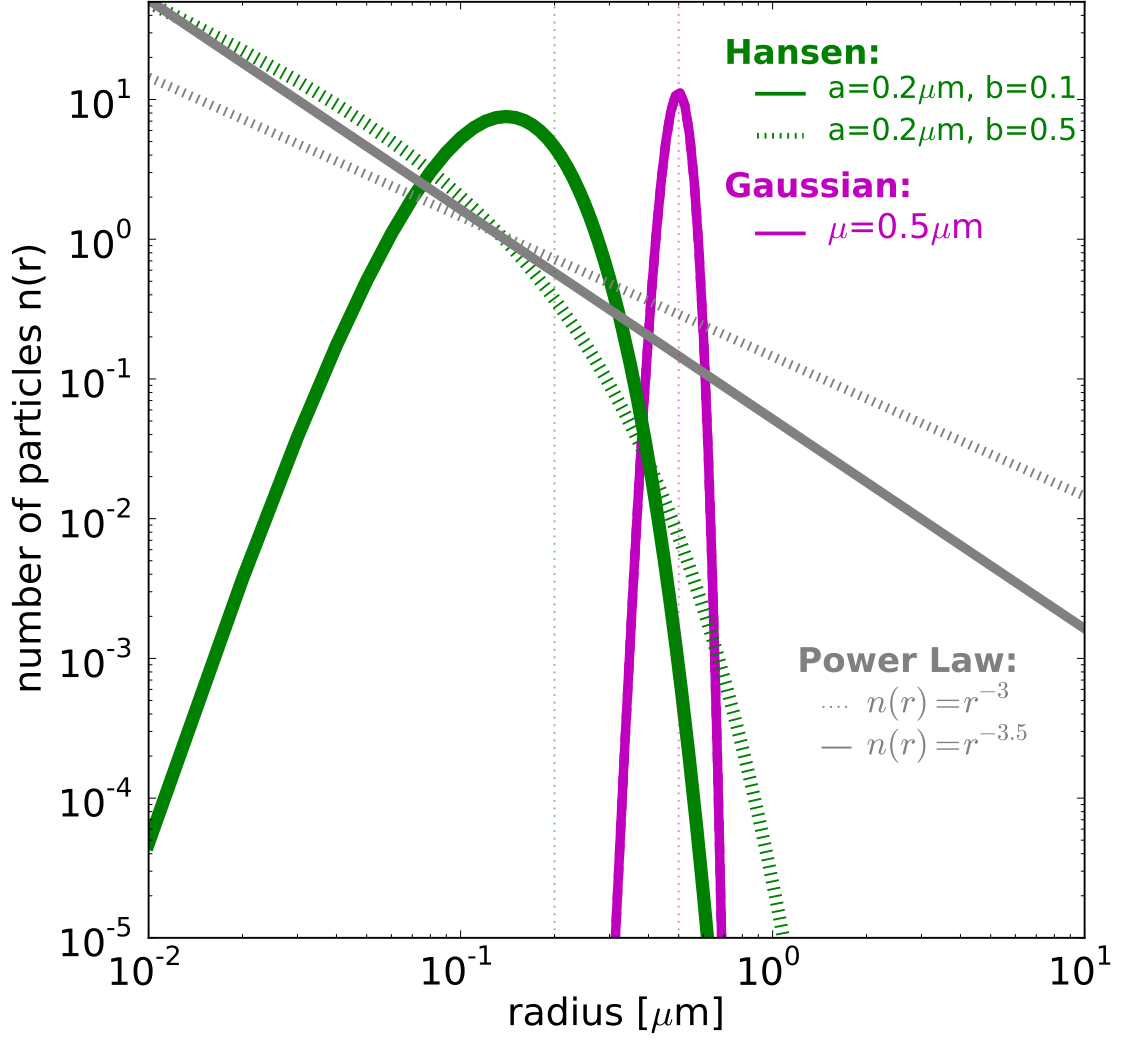


Fig. 3.— Comparison of different particle size distributions. The gray lines are the power law distributions with power indices of -3 and -3.5. The magenta is a Gaussian distribution with characteristic grain size of $0.5\ \mu\text{m}$. The green lines are Hansen distributions for $a = 0.2\ \mu\text{m}$ and $b = 0.1, 0.5$.

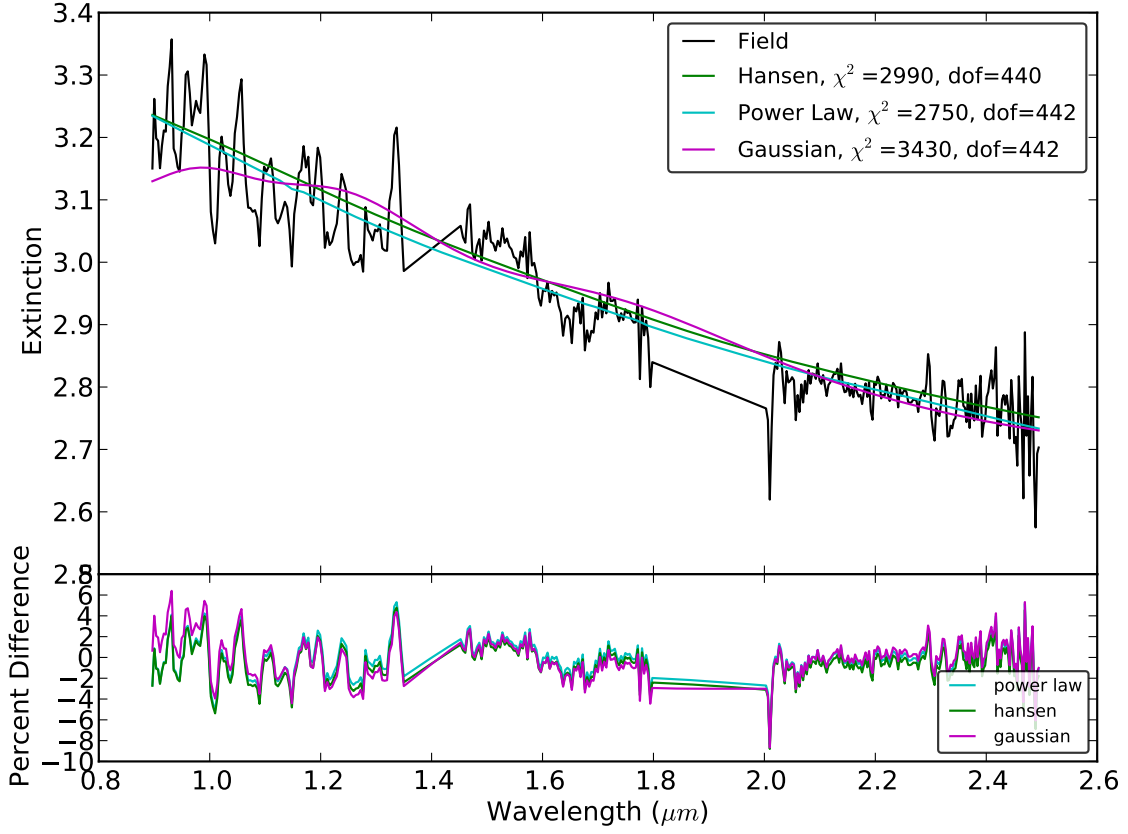


Fig. 4.— Top panel shows best-fit models with three different particle size distributions. The black line is the observed reddening with the telluric bands removed, and the colored lines are the best-fit models. Bottom panel shows the percent difference between each model and the observed reddening.

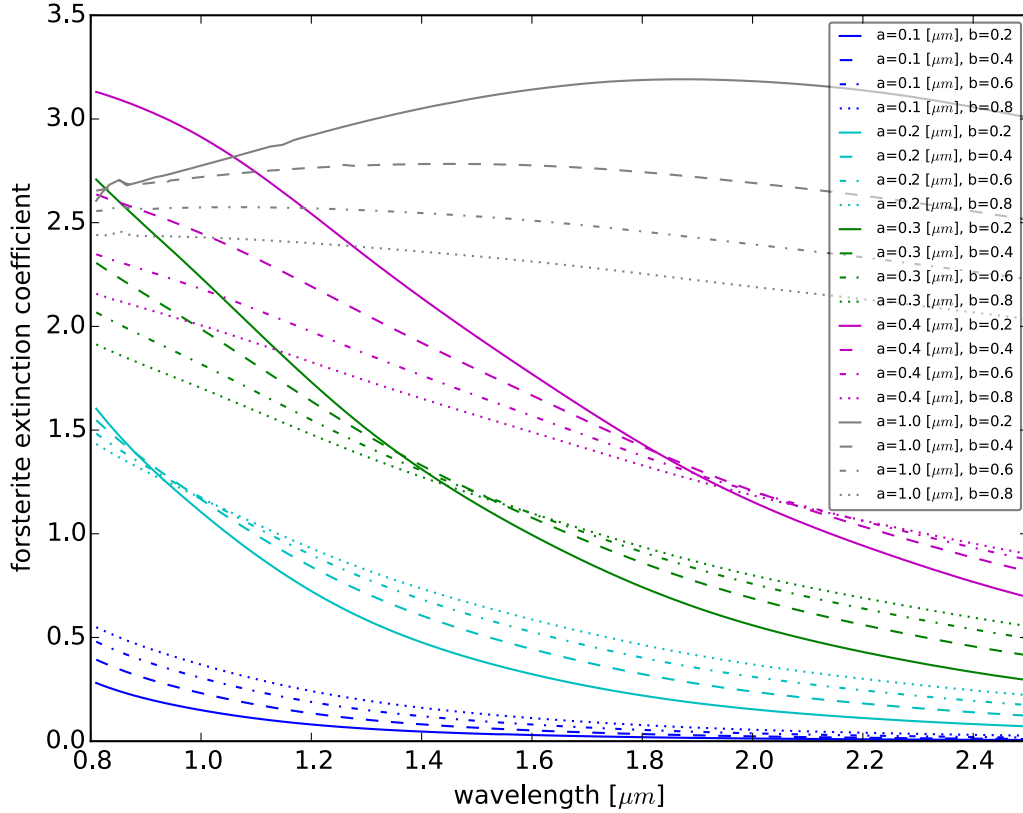


Fig. 5.— Forsterite extinction coefficients according to Mie theory averaged over Hansen particle size distributions with various combinations of mean effective particle radius (a) and effective variance (b). Different colors correspond to different effective particle radii. Different line style correspond to different effective variance. The shapes of the extinction curves for smaller particles ($0.1 - 0.4 \mu\text{m}$) resemble the observed reddening while the $1.0 \mu\text{m}$ particles do not.

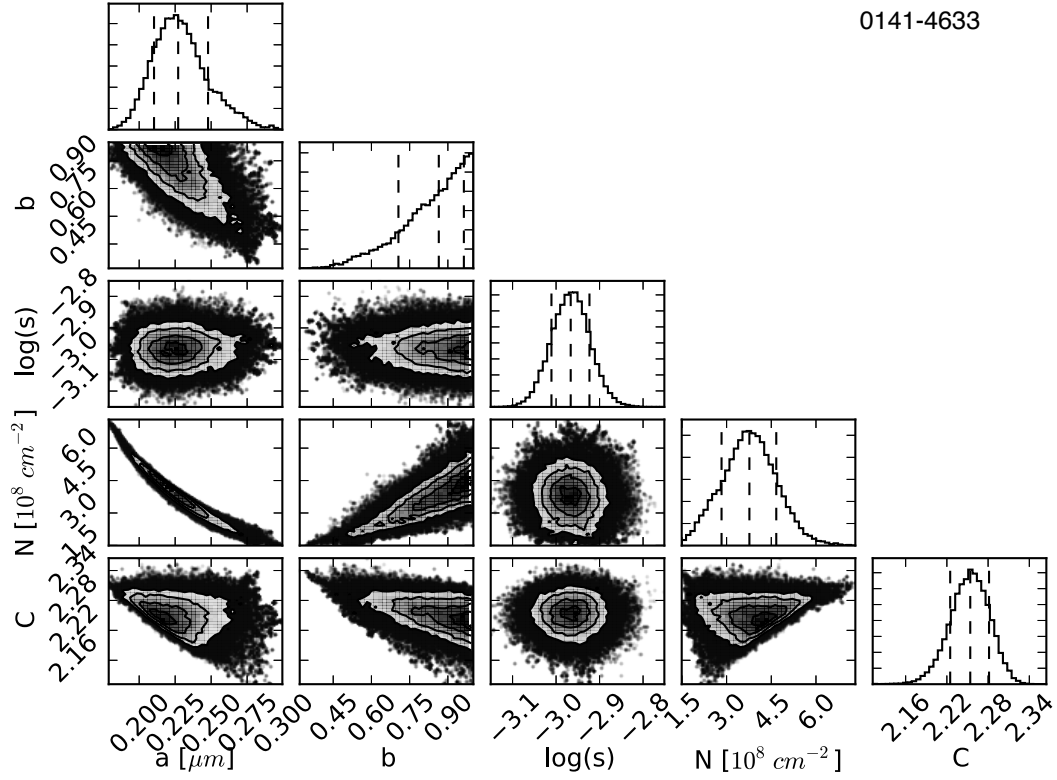


Fig. 6.— Posterior distributions of mean effective radius, effective variance, tolerance, column density, and offset showing 1-D distributions for each parameter and 2-D distributions for each combination of parameters. Dashed lines in the 1-D distributions represent 16, 50, 84 percent quantiles, corresponding to the median and 1σ uncertainties.

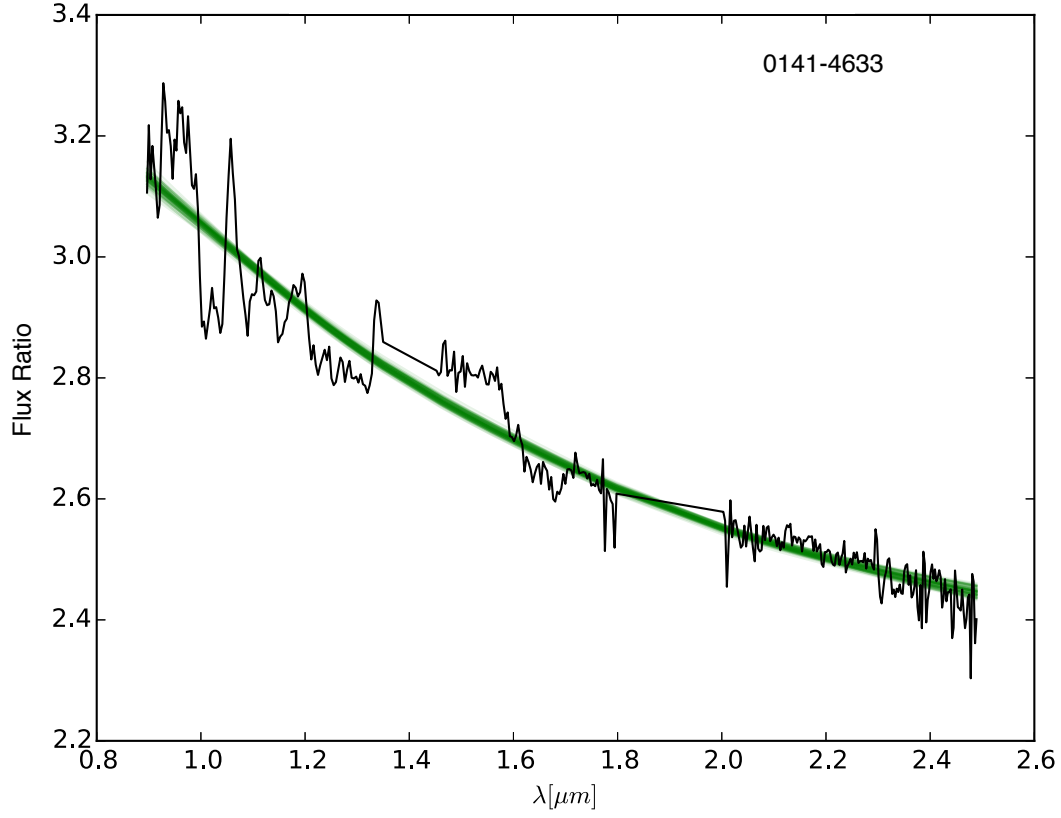


Fig. 7.— Green lines are 100 models randomly drawn from the posterior distribution overplotted on the observed reddening in black. The telluric bands ($1.35\text{--}1.45\text{ }\mu\text{m}$ and $1.8\text{--}2.0\text{ }\mu\text{m}$) are removed. The models reproduce the overall shape of the observed reddening well.

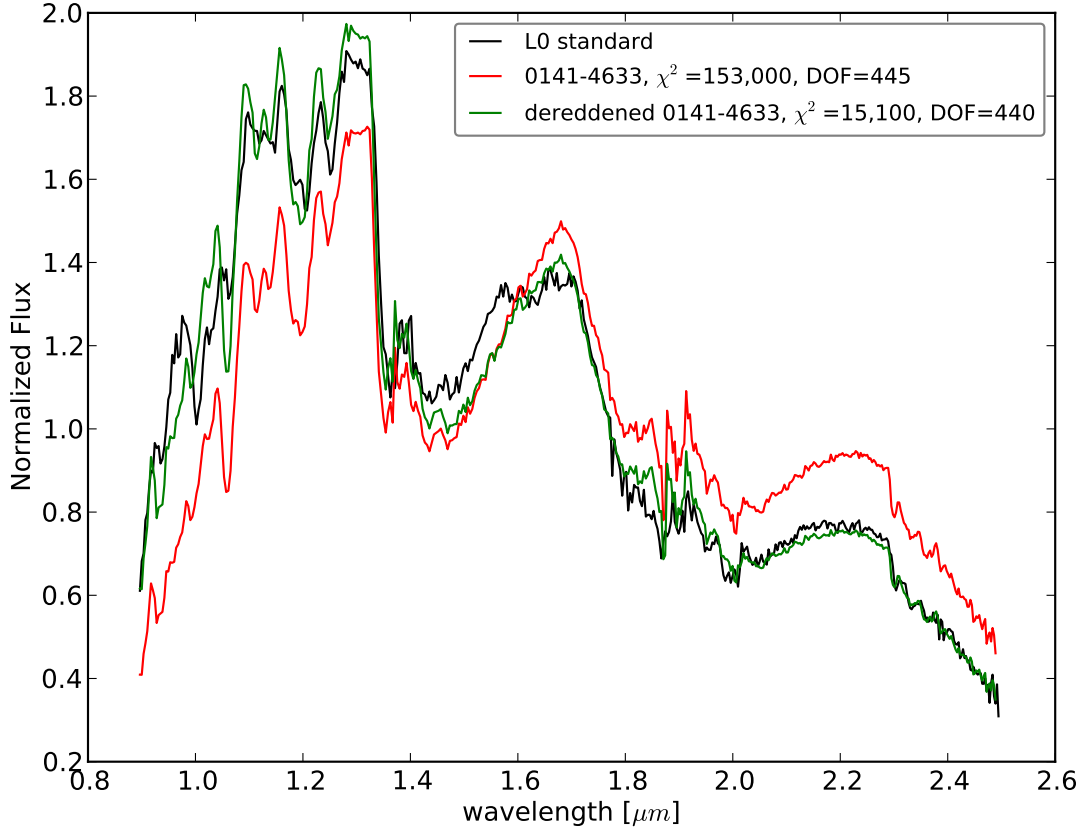


Fig. 8.— The spectrum of a red L dwarf de-reddened by the dust haze prescription is compared to the spectra of the field standard object. Black is the standard, red is the red object, and green is the spectrum of the red object de-reddened by the forsterite extinction curve for the best fit parameters from MCMC fits. χ^2 values before and after the de-reddening are also shown. The de-reddened spectrum fits the standard spectrum much better and has a smaller χ^2 value than the original red spectrum. This shows that the proposed dust haze prescription successfully corrects the red NIR slopes of red L dwarfs to look like the standard object.

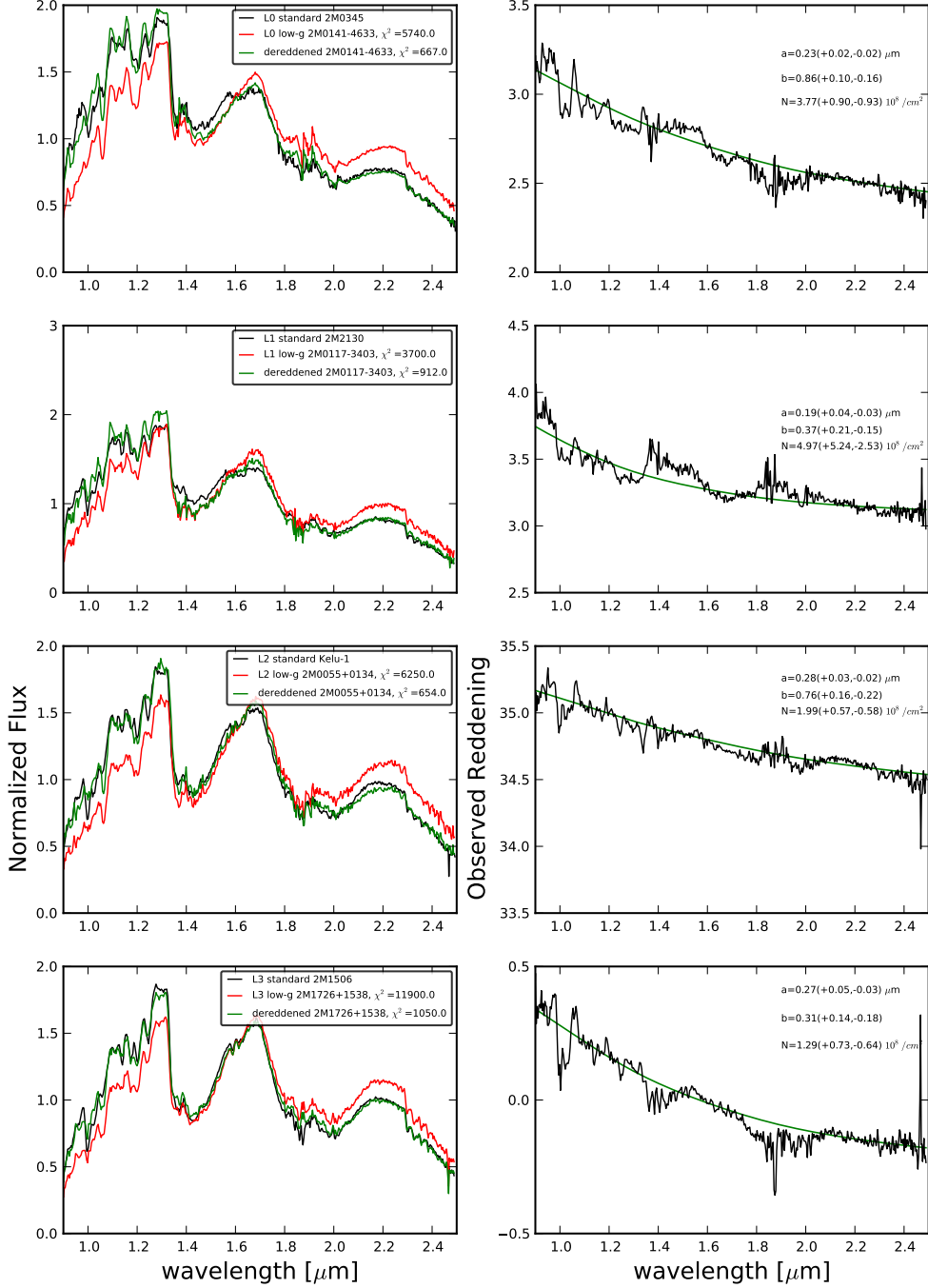


Fig. 9.— An example of de-reddened spectra (equivalent to Figure Set 8) and model fits (equivalent to Figure Set 7) for spectral types L0–L3. The left column shows the spectral standard (black), the red L dwarf (red), and the de-reddened (green) spectra. The right column shows the best-fit model (green) and the observed reddening (black).

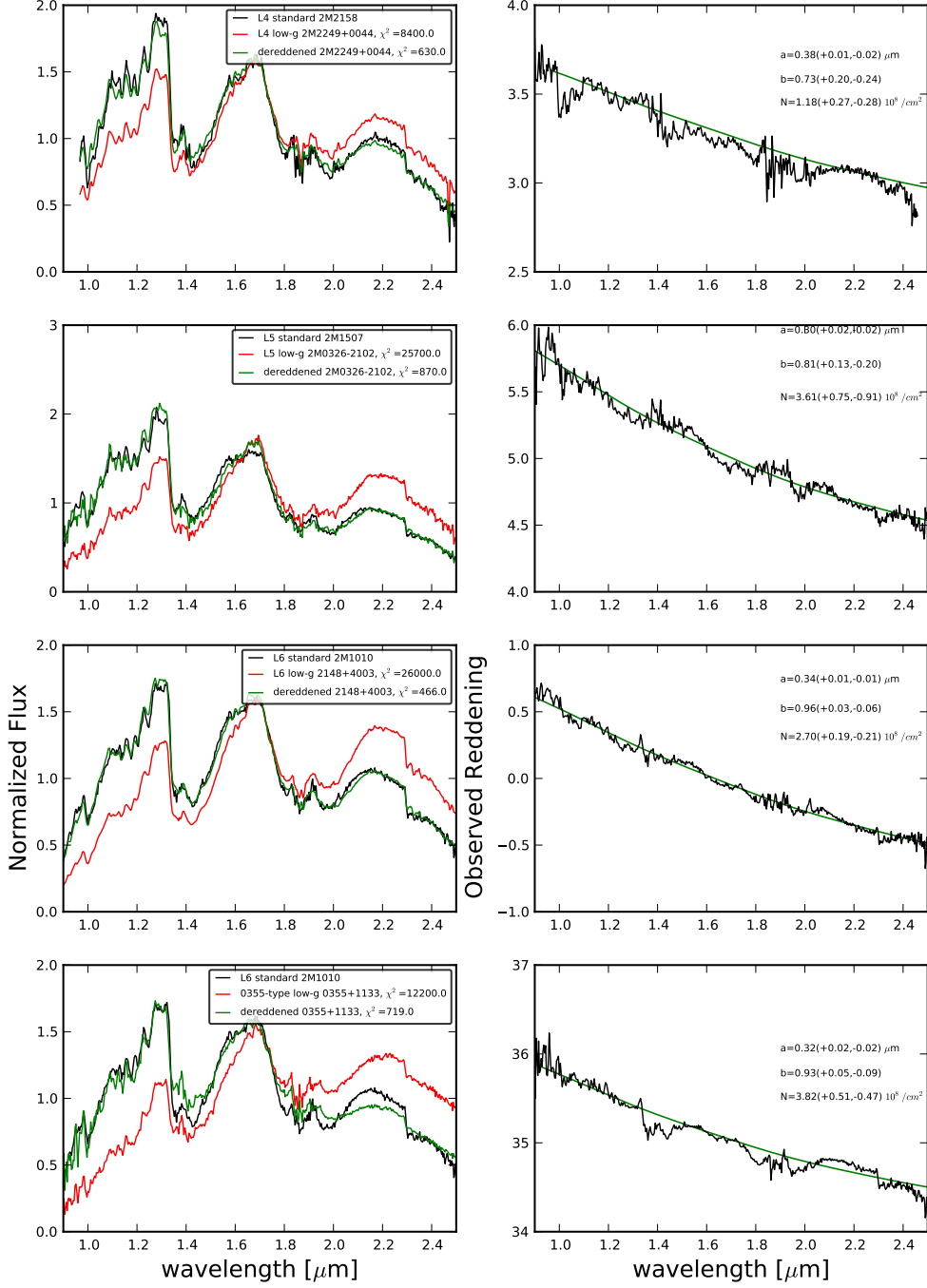


Fig. 9.2.— Same as Figure 9 for spectral types L4–L6 including 0355-type. The left column shows the spectral standard (black), the red L dwarf (red), and the de-reddened (green) spectra. The right column shows the best-fit model (green) and the observed reddening (black).

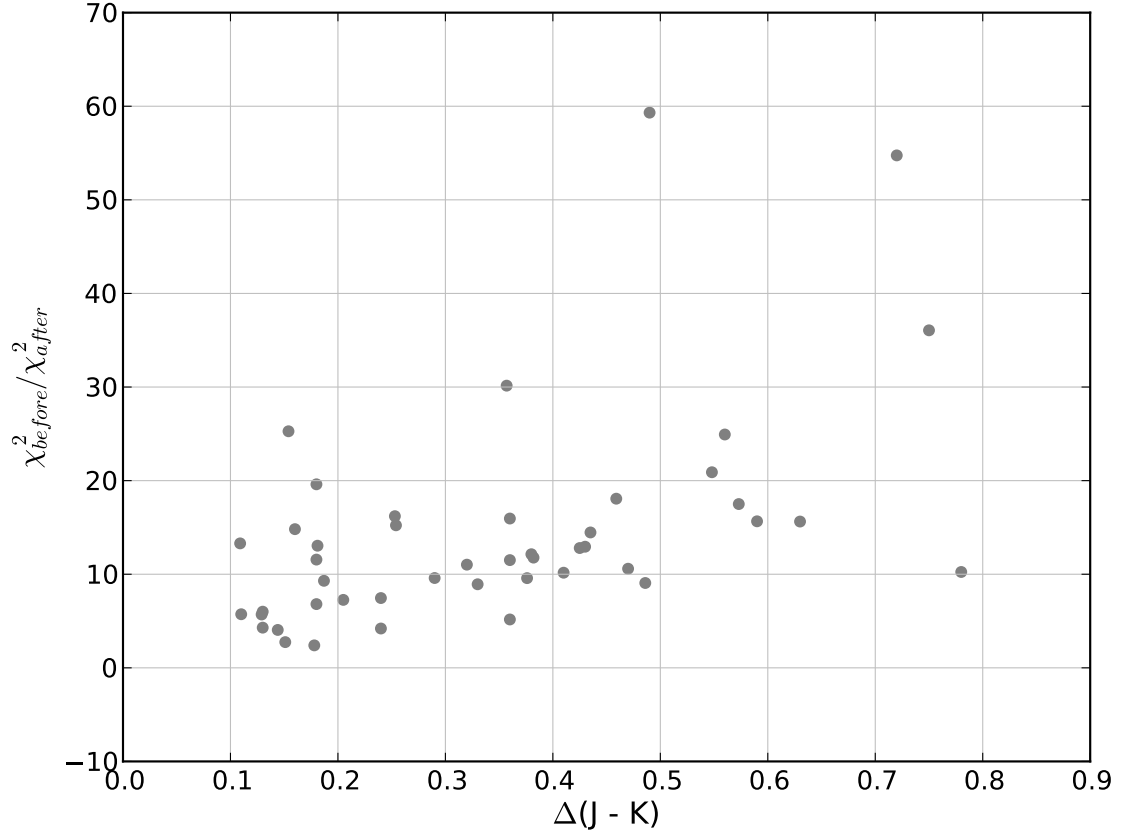


Fig. 10.— Improvement on χ^2 due to the dust haze prescription. The ratio of χ^2_{before} to χ^2_{after} is plotted against $\Delta(J - K)$ color. χ^2_{before} is χ^2 between standard and red L dwarf spectra, and χ^2_{after} is χ^2 between standard and corrected red L dwarf spectra. χ^2 value is reduced after the correction for all the objects.

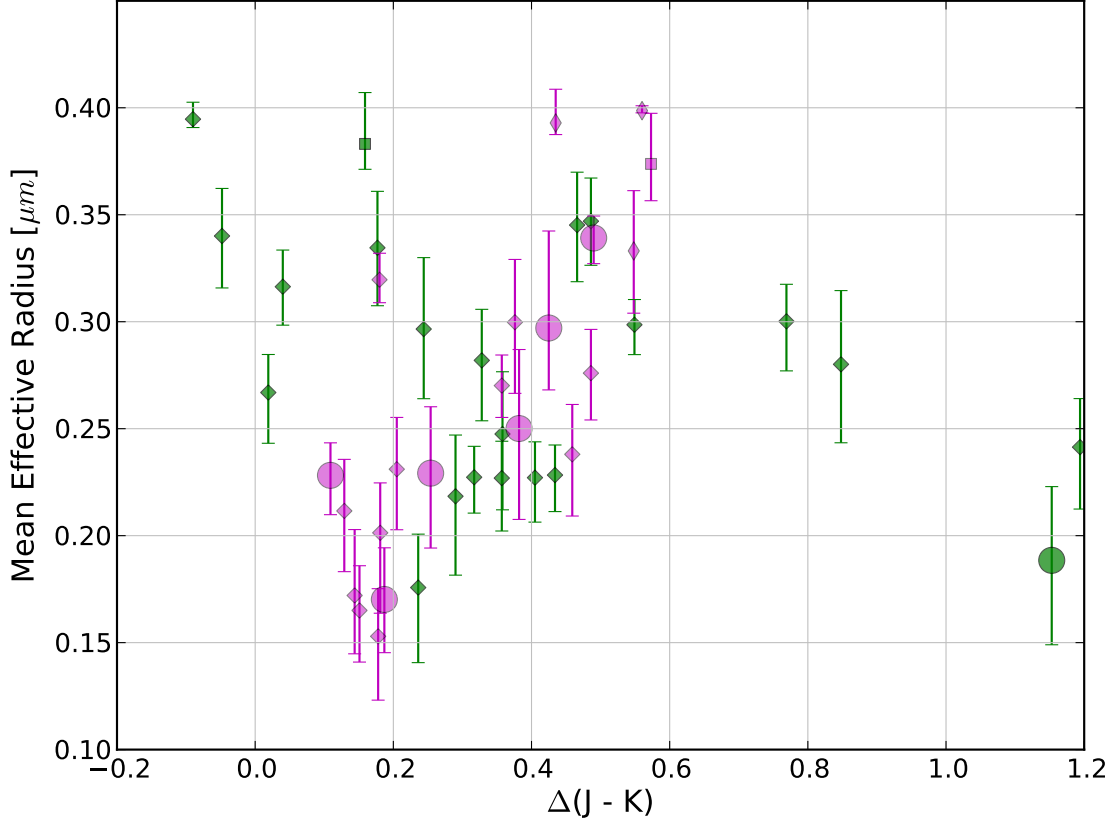


Fig. 11.— A scatter plot of mean effective radius a [μm] against $\Delta(J - K)$ color. Green markers denote low-gravity L dwarfs and magenta markers denote field-aged red L dwarfs both ranging between L0 – L5. Circles denote objects with PDFs with clear peaks. Diamonds denote objects with PDFs for b close to the limit. Thin diamonds denote objects with PDFs for a close to the limit. Squares denote objects with PDFs for both a and b close to the limits. Our sample includes object with $\Delta(J - K) > 0.1$. There appears to be a linear correlation between radius and $\Delta(J - K)$ for the field-gravity objects, while there is no noticeable trend for the low-gravity objects. The distributions of low-gravity and field-gravity objects are distinct.

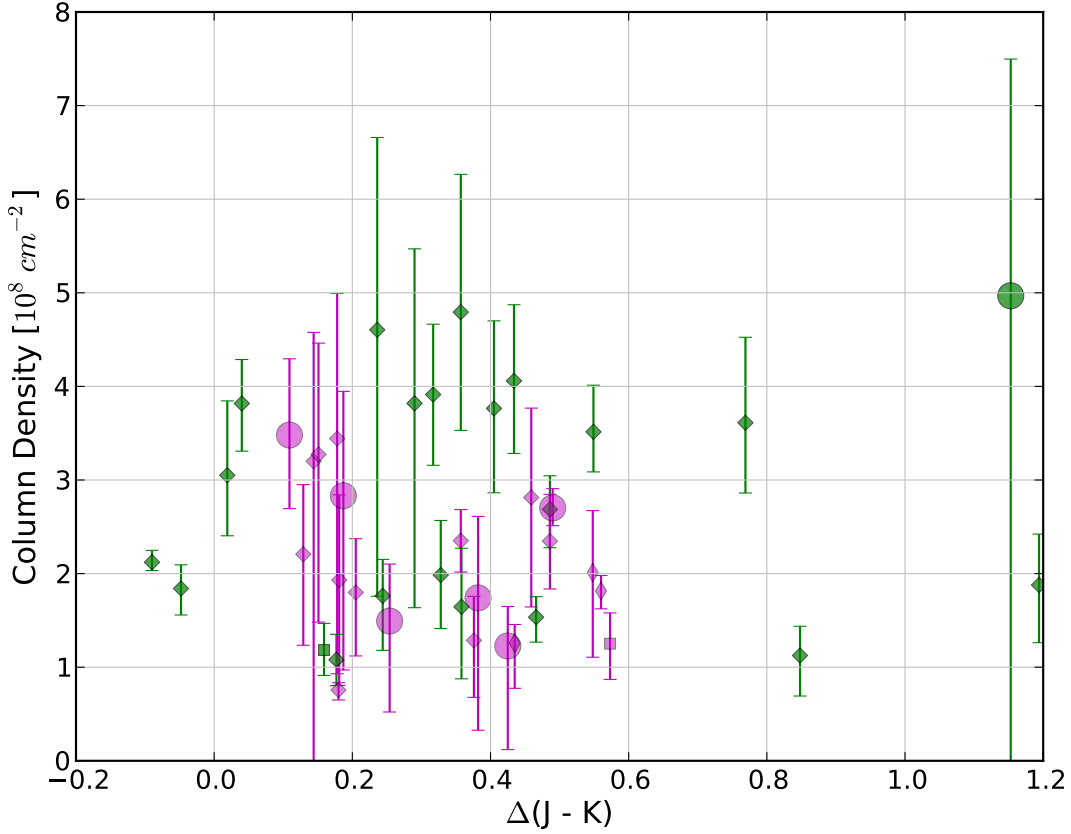


Fig. 12.— A scatter plot of column density N [10^8 cm^{-2}] against $\Delta(J - K)$ color. Green markers denote low-gravity L dwarfs and magenta markers denote field-aged red L dwarfs both ranging between L0 – L5. Circles denote objects with PDFs with clear peaks. Diamonds denote objects with PDFs for b close to the limit. Thin diamonds denote objects with PDFs for a close to the limit. Squares denote objects with PDFs for both a and b close to the limits. Our sample includes object with $\Delta(J - K) > 0.1$. The field-gravity objects appear to have lower column densities than the low-gravity objects. There is no visible trend in column density in relation to $\Delta(J - K)$ color for both low-gravity and field-gravity objects.

Table 1. L dwarfs used in this paper

2MASS Designation	Sp. Type Type	2MASS $J - K_s$	2MASS $\Delta(J - K_s)^a$	Discovery Reference	Spectral Type Reference	SpeX Prism Reference	SpeX Prism Observation Date
Spectral Standard L Dwarfs							
0345432+254023	L0	1.33	0	Kirkpatrick et al. (1997)	Kirkpatrick et al. (1999)	Burgasser and McEwain (2006)	
2130446-084520	L1	1.33	0	Kirkpatrick et al. (2008)	Kirkpatrick et al. (2008)	Kirkpatrick et al. (2010)	
13054019-2541059	L2	1.67	0	Ruiz et al. (1997)	Kirkpatrick et al. (1999)	Burgasser (2007)	
1506544+132106	L3	1.63	0	Gizis et al. (2000)	Gizis et al. (2000)	Burgasser (2007)	
21580457-1550098	L4	1.86	0	Kirkpatrick et al. (2008)	Kirkpatrick et al. (2008)	Kirkpatrick et al. (2010)	
1507476-162738	L5	1.46	0	Reid et al. (2000)	Kirkpatrick et al. (2000)	Burgasser (2007)	
10101480-0406499	L6	1.89	0	Cruz et al. (2003)	Cruz et al. (2003)	Reid et al. (2006)	
Low-gravity L Dwarfs							
01415823-4633574	L0 γ	1.74	0.410	Kirkpatrick et al. (2006)	Cruz et al. (2009)	Kirkpatrick et al. (2006)	
00325584-4405058	L0 γ	1.51	0.178	Goldman et al. (1999)	Cruz et al. (2009)	Bardalez Gagliuffi et al. (2014)	2003 Sep 04
02103857-3015313	L0 γ	1.57	0.236	Cruz et al. in prep	Cruz et al. in prep	This Paper	2006 Aug 21
0241115-032658	L0 γ	1.76	0.434	Cruz et al. (2007)	Cruz et al. (2009)	This Paper	2007 Nov 13
03231002-4631237	L0 γ	1.69	0.357	Reid et al. (2008)	Cruz et al. (2007)	This Paper	
2213449-213607	L0 γ	1.62	0.290	Cruz et al. (2007)	Cruz et al. (2009)	Bardalez Gagliuffi et al. (2014)	
23153135+0617146	L0 γ	1.80	0.466	Cruz et al. in prep	Cruz et al. in prep	This Paper	2007 Nov 14
1711135+232633	L0 γ	1.44	0.113	Cruz et al. (2007)	Cruz et al. in prep	This Paper	2008 Jul 13
15525906+2948485	L0 β	1.46	0.126	Wilson et al. (2003)	Cruz et al. (2009)	Bardalez Gagliuffi et al. (2014)	
03572695-4417305	L0 β	1.46	0.127	Bouy et al. (2003)	Cruz et al. (2009)	Bardalez Gagliuffi et al. (2014)	
0117474-340325	L1 γ	1.69	0.358	Cruz et al. (2003)	Gagne et al. (2015)	This Paper	2006 Aug 21
0518461-275645	L1 γ	1.65	0.317	Cruz et al. (2007)	Gagne et al. (2015)	Bardalez Gagliuffi et al. (2014)	
00550564+0134365	L2 γ	2.00	0.328	Cruz et al. in prep	Cruz et al. in prep	This Paper	2003 Sep 04
0536199-192039	L2 γ	1.91	0.244	Cruz et al. (2007)	Gagne et al. (2015)	This Paper	2003 Sep 03
15515237+0941148	L3: γ	2.01	0.149	Reid et al. (2008)	Gagne et al. (2015)	This Paper	2008 Jul 13
1726000+153819	L3.5 γ	1.81	0.380	Kirkpatrick et al. (2000)	Allers & Liu (2013)	Bardalez Gagliuffi et al. (2014)	
05012406-0010452	L4 γ	2.02	0.159	Reid et al. (2008)	Cruz et al. (2009)	Filippazzo et al. (2015)	
22495345+0044046	L4 γ	2.22	0.369	Geballe et al. (2002)	Gagne et al. (2015)	Allers et al. (2010)	
05120636-2949540	L5 γ	2.18	0.718	Cruz et al. (2003)	Gagne et al. (2015)	Bardalez Gagliuffi et al. (2014)	
03264225-21020572	L5 β/γ	2.21	0.752	Gizis et al. (2003)	Gagne et al. (2015)	This Paper	2007 Nov 13
21543454-1055308	L5 β/γ	2.24	0.381	Gagne et al. (2014)	Gagne et al. (2015)	This Paper	2003 Aug 11

Table 1—Continued

2MASS Designation	Sp. Type Type	2MASS $J - K_s$	2MASS $\Delta(J - K_s)^a$	Discovery Reference	Spectral Type Reference	SpeX Prism Reference	SpeX Prism Observation Date
03552337+1133437	0355-type ^b	2.52	1.06	Reid et al. (2008)	Gagne et al. (2015)	Faherty et al. (2013)	
1615425+495321	0355-type ^b	2.48	0.623	Cruz et al. (2007)	Gagne et al. (2015)	This Paper	2005 Mar 23
Red field L dwarfs							
02355993-2331205	L1	1.48	0.154	Burgasser (2008a)	Gizis et al. (2001)	Burgasser (2008a)	
05431887+6422528	L1	1.52	0.187	Reid et al. (2008)	Reid et al. (2008)	Bardalez Gagliuffi et al. (2014)	
06022216+6336391	L1:	1.58	0.263	Reid et al. (2008)	Reid et al. (2008)	Bardalez Gagliuffi et al. (2014)	
00165953-4056541	L3	1.88	0.254	Kirkpatrick et al. (2008)	Kirkpatrick et al. (2008)	Burgasser et al. (2010b)	
23392527+3507165	L3.5	1.77	0.144	Reid et al. (2008)	Reid et al. (2008)	This Paper	2003 Sep 04
11000965+4957470	L3.5	1.81	0.178	Reid et al. (2008)	Reid et al. (2008)	This Paper	2004 Nov 08
00511078-1544169	L3.5	1.81	0.181	Kirkpatrick et al. (2000)	Kirkpatrick et al. (2000)	Burgasser et al. (2010a)	
23174712-4838501	L4pec	1.97	0.109	Reid et al. (2008)	Reid et al. (2008)	Kirkpatrick et al. (2010)	
0337036-175807	L4.5	2.04	0.180	Kirkpatrick et al. (2000)	Kirkpatrick et al. (2000)	Bardalez Gagliuffi et al. (2014)	
02082363+2737400	L5	1.84	0.382	Kirkpatrick et al. (2000)	Kirkpatrick et al. (2000)	Burgasser et al. (2010a)	
0835425-081923	L5	2.03	0.573	Cruz et al. (2003)	Cruz et al. (2003)	This Paper	2004 Nov 08
03582255-4116060	L5	2.01	0.548	Reid et al. (2008)	Reid et al. (2008)	This Paper	2007 Nov 14
09054654+5623117	L5	1.67	0.205	Reid et al. (2008)	Reid et al. (2008)	Burgasser et al. (2010a)	
12281523-1547342	L5	1.61	0.151	Delfosse et al. (1997)	Burgasser et al. (2010b)	Burgasser et al. (2010a)	
12392727+5515371	L5	1.92	0.459	Kirkpatrick et al. (2000)	Burgasser et al. (2010a)	Burgasser et al. (2010a)	
03101401-2756452	L5	1.84	0.376	Cruz et al. (2007)	Cruz et al. (2007)	Bardalez Gagliuffi et al. (2014)	
06244595-4521548	L5	1.89	0.425	Reid et al. (2008)	Reid et al. (2008)	Bardalez Gagliuffi et al. (2014)	
0652307+471034	L5	1.82	0.357	Cruz et al. (2003)	Cruz et al. (2003)	This Paper	2004 Nov 07
14383259+5722168	L5	1.59	0.129	Zhang et al. (2009)	Zhang et al. (2009)	Bardalez Gagliuffi et al. (2014)	
1326298-003831	L5	1.90	0.435	Fan et al. (2000)	Cruz et al. (2003)	Geballe et al. (2002)	
22120703+3430351	L5:	1.95	0.486	Reid et al. (2008)	Reid et al. (2008)	This Paper	2004 Sep 05
21481633+4003594	L6	2.38	0.49	Looper et al. (2008)	Looper et al. (2008)	Looper et al. (2008)	
22443167+2043433	L6.5	2.45	0.56	Dahn et al. (2002)	Kirkpatrick et al. (2008)	Looper et al. (2008)	

^a $\Delta J - K_s$ is the difference in $J - K_s$ colors between the red L dwarf and the corresponding spectral standard object.

^b0355-type objects are defined by Gagne et al. (2015). A conservative estimate of L3–L6 γ is adopted for the spectral type range. For our analysis, 0355-type objects are compared to the L6 spectral standard object.